

Decomposition mechanisms and non-isothermal kinetics of $\text{LiHC}_2\text{O}_4 \cdot \text{H}_2\text{O}$

LI Dong, LIAN Fang, and CHOU Kuo-Chih

School of Materials Science and Engineering, University of Science and Technology Beijing, Beijing 100083, China

Received 7 March 2012; received in revised form 2 July 2012; accepted 12 July 2012

© The Nonferrous Metals Society of China and Springer-Verlag Berlin Heidelberg 2012

Abstract

The thermal decomposition process of $\text{LiHC}_2\text{O}_4 \cdot \text{H}_2\text{O}$ from 30 to 600 °C was investigated by the thermogravimetric and differential scanning calorimetry (TG-DSC). The phases decomposed at different temperature were characterized by X-ray diffraction (XRD), which indicated the decompositions at 150, 170, and 420 °C, relating to LiHC_2O_4 , $\text{Li}_2\text{C}_2\text{O}_4$, Li_2CO_3 , and Li_2CO_3 , respectively. Reaction mechanisms in the whole sintering process were determined, and the model fitting kinetic approaches were applied to data for non-isothermal thermal decomposition of $\text{LiHC}_2\text{O}_4 \cdot \text{H}_2\text{O}$; finally, the kinetic parameters of each reaction were also calculated herein.

Keywords: apparent activation energy; non-isothermal; reaction mechanism; thermal decomposition

1 Introduction

During the past decades, extensive efforts were dedicated to lithium batteries because of the high energy and power density, high safety, long cycle life, and low cost [1–7]. The cathode materials of lithium batteries were synthesized by various routes, such as ion exchange method [8–10], coprecipitation method [11–13], and solid-state method [14–17]. Among the synthesis methods, low-heating solid-state synthesis was accepted as one of the most innovative methods due to the simplicity and low energy consuming. Recently, some references reported that the cathodes were successfully prepared by the same or similar method [18–19]. However, the manufactured cathode with the same composition exhibited different values for discharge capacity and other electrochemical properties. In order to understand the mechanism behind the phenomenon and improve the electrochemical performance of cathodes, the structure has to be investigated, which depends critically on the synthesis process including the calcination process. Nevertheless, the decomposition process and corresponding intermediate product in sintering are still obscure due to multicomponent and the complex structure of precursor. In our previous research, it is confirmed that the precursor consists of $\text{LiHC}_2\text{O}_4 \cdot \text{H}_2\text{O}$, LiHC_2O_4 , and chelate obtained by low-heat solid-state reaction. To understand the reaction mechanisms of calcination and the synthesis process, the decomposition process of $\text{LiHC}_2\text{O}_4 \cdot \text{H}_2\text{O}$ and chelate was investigated herein. More-

over, decomposition products and non-isothermal kinetics of $\text{LiHC}_2\text{O}_4 \cdot \text{H}_2\text{O}$ were also given.

2 Experimental

As previously reported [20], $\text{LiHC}_2\text{O}_4 \cdot \text{H}_2\text{O}$ was prepared by dissolving $\text{H}_2\text{C}_2\text{O}_4 \cdot 2\text{H}_2\text{O}$ in hot water and adding an equivalent mole amount of Li_2CO_3 . The thermal decomposition process of the $\text{LiHC}_2\text{O}_4 \cdot \text{H}_2\text{O}$ in air was tested by TG-DSC (Germany, NETZSCH STA 449 C). Powder X-ray diffraction (XRD, Japan, Rigaku, D/max-RB, 12kW) using Cu K α radiation was employed to identify the crystalline phase of the intermediate decomposition of $\text{LiHC}_2\text{O}_4 \cdot \text{H}_2\text{O}$.

3 Results and discussion

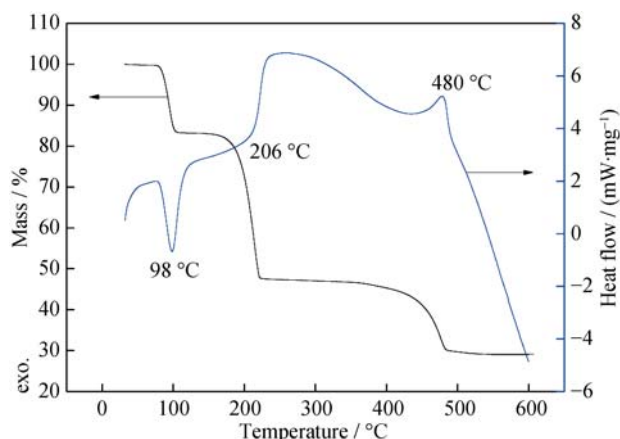
3.1 TG-DSC and XRD analysis

$\text{LiHC}_2\text{O}_4 \cdot \text{H}_2\text{O}$ was heated from 30 to 600 °C at the heating rate of 5 K·min⁻¹, of which the TG-DSC curves are shown in Fig. 1. There are obvious three mass loss stages in TG curve and values of mass loss in the different temperature range are given in Table 1.

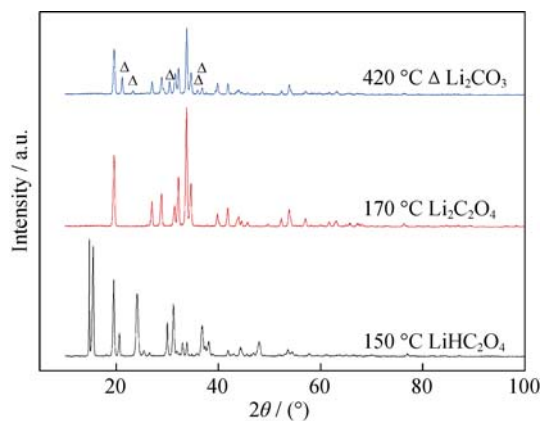
According to the TG-DSC curves, reactions occur at 75, 150, and 416 °C, respectively. To investigate the reaction mechanism and decomposition products in the whole sintering process, $\text{LiHC}_2\text{O}_4 \cdot \text{H}_2\text{O}$ was sintered at three different

Table 1 Theoretical and experimental values of mass loss for each reaction

Temperature range/°C	Reaction equation	Theory value/%	Measurement value /%
75~150	$\text{LiHC}_2\text{O}_4 \cdot \text{H}_2\text{O}(\text{s}) \rightarrow \text{LiHC}_2\text{O}_4(\text{s}) + \text{H}_2\text{O}(\text{g})$	15.8	16.0
150~416	$2\text{LiHC}_2\text{O}_4(\text{s}) \rightarrow \text{Li}_2\text{C}_2\text{O}_4(\text{s}) + \text{H}_2\text{O}(\text{g}) + \text{CO}(\text{g}) + \text{CO}_2(\text{g})$	39.5	38.6
416~500	$\text{Li}_2\text{C}_2\text{O}_4(\text{s}) \rightarrow \text{Li}_2\text{CO}_3(\text{s}) + \text{CO}(\text{g})$	13.0	14.8

**Fig. 1** TG-DSC curves of thermal decomposition of $\text{LiHC}_2\text{O}_4 \cdot \text{H}_2\text{O}$ in air, obtained at the heating rate of $5 \text{ K} \cdot \text{min}^{-1}$

temperatures. The XRD patterns of decompositions are shown in Fig. 2. The decomposition at 150°C is confirmed to be the dehydration of $\text{LiHC}_2\text{O}_4 \cdot \text{H}_2\text{O}$. The result is consistent with TG-DSC curves, and the sample heated to 170°C for 3 h is $\text{Li}_2\text{C}_2\text{O}_4$ pure phase. While there are several weak peaks in the XRD patterns (Fig. 2) of the sample after heat treated at 420°C , which are indexed to the Li_2CO_3 . A small amount of $\text{Li}_2\text{C}_2\text{O}_4$ begins to decompose, which can be confirmed from a weight loss at about 420°C in TG curve (Fig. 2). The above analysis allows us to conclude the chemical reactions and corresponding theoretical weight loss value in the whole heating process listed in Table 1. Moreover, the non-isothermal kinetic analysis was applied to investigate the kinetic characteristics in sintering process.

**Fig. 2** XRD patterns of decomposition products of $\text{LiHC}_2\text{O}_4 \cdot \text{H}_2\text{O}$ at different temperatures

3.2 Kinetic analysis

The normalized mass loss and conversion α were typically calculated from the corresponding TG curves as

$$\alpha = (m_0 - m_T) / (m_0 - m_{Te}) \quad (1)$$

where m_0 , m_T , and m_{Te} are initial sample mass, sample mass at the temperature T (the absolute temperature), and sample mass at the end of reaction, respectively.

The classical isothermal reaction rate equation is expressed as

$$d\alpha/dt = kf(\alpha) \quad (2)$$

where k is the reaction rate constant, and $f(\alpha)$ is the reaction mechanism function.

Generally, the relationship between reaction rate constant and reaction temperature should obey the Arrhenius law, that is

$$k = A \exp(-\Delta E_a/RT) \quad (3)$$

where A is the frequency factor; ΔE is the apparent activation energy; R is the gas constant; and T is the reaction temperature (the absolute temperature).

When the temperature increase is linear,

$$T = T_0 + \beta t \quad (4)$$

where β is the heating rate.

Combining Eqs. (2)–(3) yields Eq. (5)

$$d\alpha/dT = A \cdot \exp(-\Delta E_a/RT) \cdot f(\alpha)/\beta \quad (5)$$

or

$$d\alpha/f(\alpha) = A \cdot \exp(-\Delta E_a/RT) \cdot dT/\beta \quad (6)$$

The integration form of Eq. (6) can be expressed as

$$g(\alpha) = A \cdot \Delta E_a \cdot p(u)/(\beta \cdot R) \quad (7)$$

$$P(u) = -\int_{\infty}^u (e^{-u}/u^2) du \quad (8)$$

where $u = \Delta E_a/RT$. For non-isothermal conditions, there are several relationships used to calculate Arrhenius parameters, each of which is based on an approximate form of the temperature integral that results from rearrangement and integration of Eq.(7). The Coats-Redfern [21] approximation of the $p(u)$ function was applied in the study:

$$\ln[g(\alpha)/T^2] = \ln[AR \cdot (1 - 2RT/\Delta E_a)/(\beta \cdot \Delta E_a)] - \Delta E_a/(RT) \cong \quad (9)$$

$$\ln[AR/(\beta \cdot \Delta E_a)] - \Delta E_a/(RT)$$

According to Eq.(9), the plot of $\ln[g(\alpha)/T^2]$ versus $1/T$ should be a straight line, and the apparent action energy of reaction ΔE_a is obtained.

3.3 Determination of the reaction model by Malek approach

There is a single reaction within the desired temperature range, which concludes in Table 1. As reported in the Refs. [22–23], the model-fitting approach can be realized when the reaction proceeds via a single mechanism. The Malek method is reliable to determine the reaction kinetic model and is applied here. As follows, one obtains the master plots of theoretical calculation functions $y(\alpha)$ and experiment $y'(\alpha)$ as a function of α .

$$y(\alpha) = f(\alpha) \cdot g(\alpha) / [f(0.5) \cdot g(0.5)] \tag{10}$$

$$y'(\alpha) = T^2 \cdot (d\alpha/dt) / [T_{0.5}^2 \cdot (d\alpha/dt)_{0.5}] \tag{11}$$

where $g(\alpha)$ and $f(\alpha)$ correspond to theoretical master plots of various functions. The knowledge of temperature as a function of α should be known in advance to draw the experiment master plots of $y'(\alpha)$ versus α from experimental data at a given heating rate. According to the Malek method, for a given α , the experimental values $y'(\alpha)$ and theoretically calculated values $y(\alpha)$ can be equivalent or a little derivation if the reaction mechanism can be given by the appropriate kinetic model. Table 2 shows the most probable reaction mechanism functions.

The non-isothermal kinetic data of dehydration in the first weight loss stage were simulated by 14 kinetic models listed in Table 2. It can be concluded from Fig. 3 that the model 5 is appropriate for describing the dehydration process (the first reaction), in conversion range of $0.05 \leq \alpha \leq 0.9$. The inte-

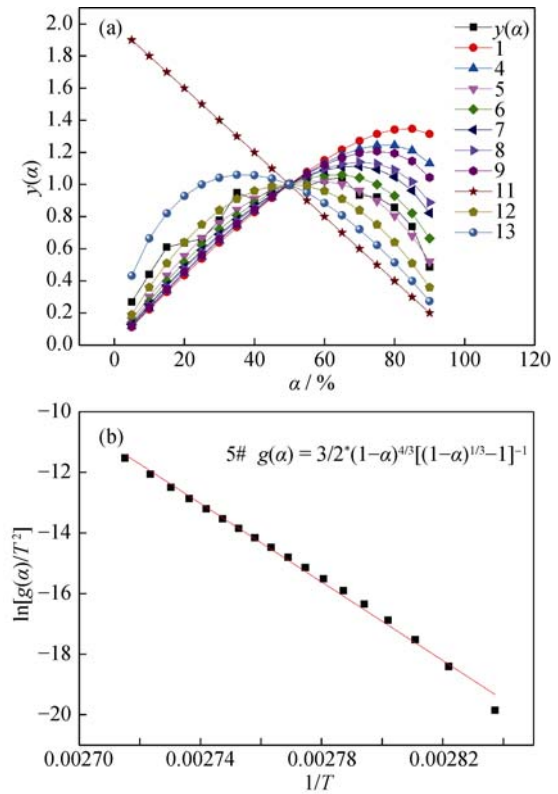


Fig. 3 (a) Plots of theoretical values $y'(\alpha)$ and experimental values $y(\alpha)$ versus α for the dehydration of $\text{LiHC}_2\text{O}_4 \cdot \text{H}_2\text{O}$; (b) Plots of $\ln[g(\alpha)/T^2]$ versus $1/T$ with model 5

gral form of model 5, conversion α , and the corresponding T are substituted into Eq.(9), and the apparent activation energy of the first reaction $\Delta E_{a1} = 538 \text{ kJ} \cdot \text{mol}^{-1}$ can be obtained.

Table 2 Most probable reaction functions for three reactions

Nos.	Function name	Integral function $g(\alpha)$	Differential function $f(\alpha)$
1	Valensi	$\alpha + (1 - \alpha)\ln(1 - \alpha)$	$[-\ln(1 - \alpha)]^{-1}$
2	Jander $n=1/2$	$[1 - (1 - \alpha)^{1/2}]^{1/2}$	$4(1 - \alpha)^{1/2}[1 - (1 - \alpha)^{1/2}]^{1/2}$
3	Jander $n=2$	$[1 - (1 - \alpha)^{1/2}]^2$	$(1 - \alpha)^{1/2}[1 - (1 - \alpha)^{1/2}]^{-1}$
4	Ginstling-Brounshtein	$1 - 2\alpha/3 - (1 - \alpha)^{2/3}$	$3[(1 - \alpha)^{1/3} - 1]^{-1} / 2$
5	Zhuralev-L-Tempelman	$[(1 - \alpha)^{1/3} - 1]^2$	$3(1 - \alpha)^{4/3} [(1 - \alpha)^{-1/3} - 1]^{-1} / 2$
6	Avrami-Erofeev Eq.	$-\ln(1 - \alpha)$	$1 - \alpha$
7	Three-quarters order	$1 - (1 - \alpha)^{1/4}$	$4(1 - \alpha)^{3/4}$
8	Two-third order	$1 - (1 - \alpha)^{1/3}$	$3(1 - \alpha)^{2/3}$
9	One-second order	$[1 - (1 - \alpha)^{1/2}]$	$2(1 - \alpha)^{1/2}$
10	Contracting sphere	$2[1 - (1 - \alpha)^{1/2}]$	$(1 - \alpha)^{1/2}$
11		$(1 - \alpha)^{-1}$	$(1 - \alpha)^2$
12	Second order	$(1 - \alpha)^{-1} - 1$	$(1 - \alpha)^2$
13	Exponential law	$\ln \alpha$	α
14		$1 - (1 - \alpha)^2$	$(1 - \alpha)^{-1} / 2$

The same analysis is applied to the second and third reactions. It is shown that there are four appropriate models for the second reaction in Figs.4 (a) and 5. To discern the kinetic model of the second reaction, the thermogravimetric data and four different kinetic models (2, 3, 9, and 10) are substituted into Eq.(9). The coefficient of determination (r^2) of linear regression in Table 3 shows the best result of linearization procedure for process handled by model 3 with the apparent activation energy $\Delta E_{a_2} = 292 \text{ kJ}\cdot\text{mol}^{-1}$.

For the third reaction, Fig. 6 shows that the experimental master plots of $y'(\alpha)$ versus α is in good agreement with the theoretical master plots of $y'(\alpha)$ versus α corresponding to model 14. In Fig. 6(c), one can calculate the third reaction apparent energy, $\Delta E_{a_3} = 54 \text{ kJ}\cdot\text{mol}^{-1}$.

It has been known that precursor prepared by low-heating solid-state method consists of $\text{LiHC}_2\text{O}_4\cdot\text{H}_2\text{O}$, LiHC_2O_4 , and chelate. In view of the complex structure and thermal decomposition process of chelate, the investigation of $\text{LiHC}_2\text{O}_4\cdot\text{H}_2\text{O}$ thermal decomposition mechanism is very important in order to understand the decomposition mechanisms of precursor. The decomposition mechanism of $\text{LiHC}_2\text{O}_4\cdot\text{H}_2\text{O}$ and kinetic parameters corresponding to each reaction in sintering are given in the paper. The results suggest the thermal decomposition mechanism of precursor prepared by low-heating solid-state method and especially provide an important route for analysis of thermal decompo-

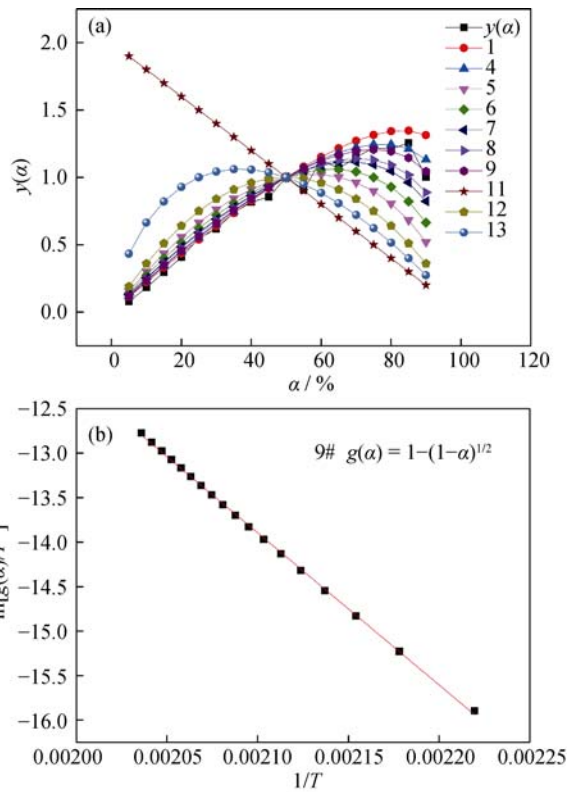


Fig. 4 (a) Plots of theoretical functions $y'(\alpha)$ and experiment $y(\alpha)$ versus α for the second reaction; and (b) plots of $\ln[g(\alpha)/T^2]$ versus $1/T$ with model 9

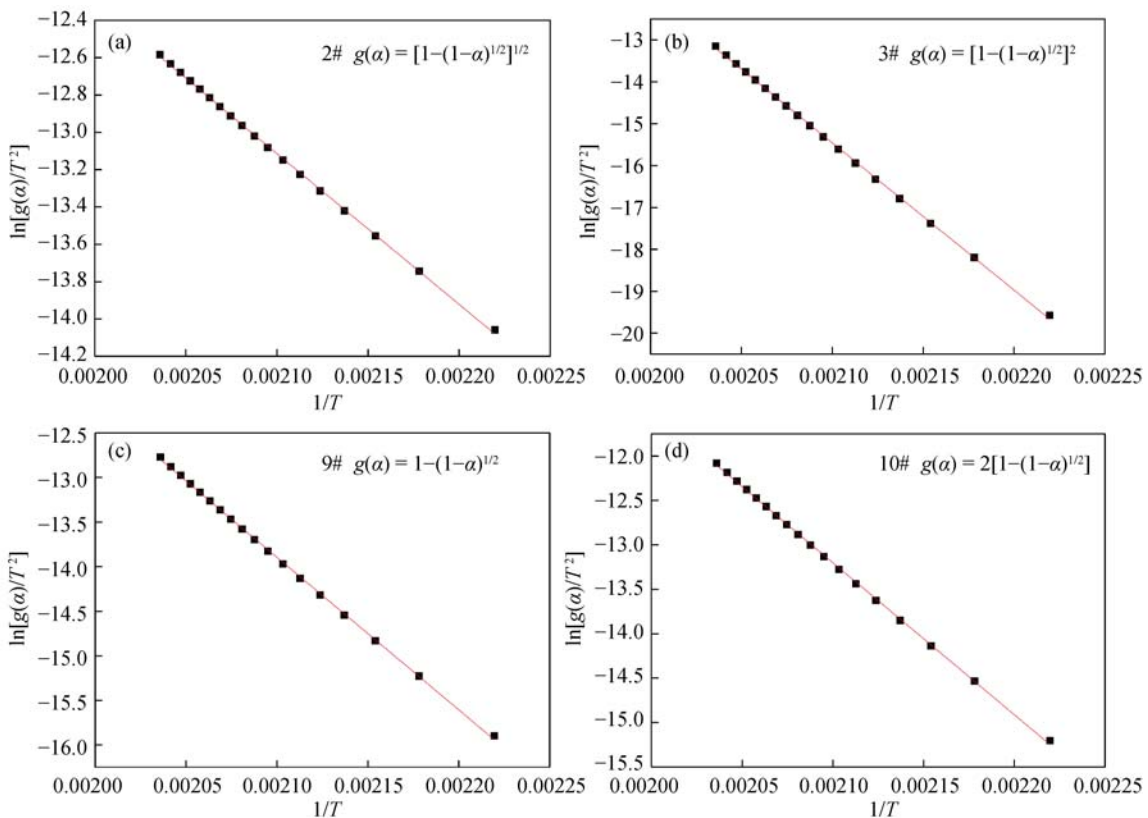


Fig. 5 Plots of $\ln[g(\alpha)/T^2]$ versus $(1/T)$ with model 2, 3, 9, and 10

Table 3 Coefficient of determination (*r*²) of linear regression with different models

Model	2#	3#	9#	10#
Correlation	0.99953	0.99956	0.99955	0.99955

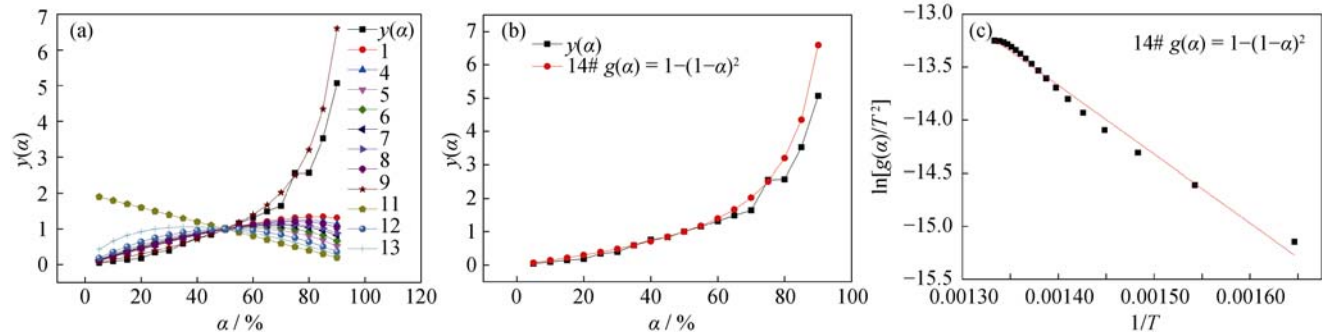


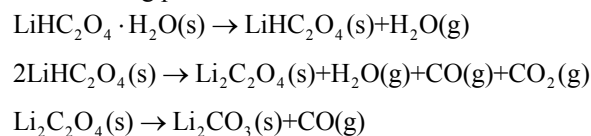
Fig. 6 (a) Plots of theoretical functions *y'*(α) and experiment *y*(α) versus α for third reaction; (b) Plots of theoretical functions *y'*(α) with model 14 and experiment *y*(α) versus α for third reaction; (c) Plots of $\ln[g(\alpha)/T^2]$ versus $1/T$ with model 14.

sition process of other oxalates and dioxalates. The thermal decomposition process of chelate would be discussed in the following investigation.

4 Conclusion

The thermal decomposition process of LiHC₂O₄·H₂O from 30 to 600 °C was studied by the TG-DSC. There are three decomposition reactions occurring at about 75, 150, and 416 °C, and the decomposition products at 150, 170, and 420 °C relate to LiHC₂O₄, Li₂C₂O₄, Li₂C₂O₄, and Li₂CO₃, respectively.

Three decomposition reactions can be concluded in the whole heating process as follows:



The reaction kinetic model 5, 3, and 14 are confirmed to the corresponding first, second, and third weight loss stage from 30 to 600 °C, of which the apparent activation energy is 532, 292, and 54 kJ·mol⁻¹, respectively.

Acknowledgements

This work was financially supported by the National “863” Program of China (No.2009AA03Z226), Project on the Integration of Industry, Education and Research of Guangdong Province (No.2011A090200012) and the Fundamental Research Funds for the Central Universities (No.FRF-MP-12-005B).

References

[1] Ohzuku T., Kitano S., Iwanaga M., Matsuno H., and Ueda A.,

Comparative study of Li[Li_xMn_{2-x}]O₄ and LT-LiMnO₂ for lithium-ion batteries, *J. Power Sources*, 1997, **68** (2): 646.
 [2] Thackeray M.M., Mansuetto M.F., and Bates J.B., Structural stability of LiMn₂O₄ electrodes for lithium batteries, *J. Power Sources*, 1997, **68** (1): 153.
 [3] Ceder G., Chiang Y.M., Sadoway D.R., Aydinol M.K., Jang Y.I., and Huang B., Identification of cathode materials for lithium batteries guided by first-principles calculations, *Nature*, 1998, **392**: 694.
 [4] Tarascon J.M., and Armand M., Issues and challenges facing rechargeable lithium batteries, *Nature*, 2001, **414**: 359.
 [5] Meng Y.S., Ceder G., Grey C.P., Yoon W.S., Jiang M., Bréger J., and Shao-Horn Y., Cation ordering in layered O₃ Li[Ni_xLi_{1/3-2x/3}Mn_{2/3-x/3}]O₂ (0 ≤ x ≤ 1/2) compounds, *Chem. Mater.*, 2005, **17** (9): 2386.
 [6] Armstrong A.R., Lyness C., Panchmatia P.M., Saiful M., and Bruce P.G., The lithium intercalation process in the low-voltage lithium battery anode Li_{1-x}V_{1-x}O₂, *Nat. Mater.*, 2011, **10**: 223.
 [7] Li X.W., Lin Y.B., Lin Y., Lai H., and Huang Z.G., Surface modification of LiNi_{1/3}Co_{1/3}Mn_{1/3}O₂ with Cr₂O₃ for lithium ion batteries, *Rare Metals*, 2012, **31** (2): 140.
 [8] Armstrong A.R., Paterson A.J., Dupre N., Grey C.P., and Bruce P.G., Structural evolution of layered Li_xMn_yO₂: combined neutron, NMR, and electrochemical study, *Chem. Mater.*, 2007, **19** (5): 1016.
 [9] Gregory Becht A., John Vaughey T., Britt Robin L., Eagle Cassandra T., and Hwu S.J., Ion exchange and electrochemical evaluation of the microporous phosphate Li₉Fe₇(PO₄)₁₀, *Mater. Res. Bull.*, 2008, **43** (12): 3389.
 [10] Hirayama M., Tomita H., Kubota K., and Kanno R., Structure and electrode reactions of layered rocksalt LiFeO₂ nanoparticles for lithium battery cathode, *J. Power Sources*, 2011, **196** (16): 6809.
 [11] Li L.-j., Li X.-h., Wang Z.-x., Guo H.-j., Yue P., Chen W., and Wu L., A simple and effective method to synthesize layered LiNi_{0.8}Co_{0.1}Mn_{0.1}O₂ cathode materials for lithium ion

- battery, *Powder Technol.*, 2011, **206** (3): 353.
- [12] Tabuchi M., Nabeshima Y., Ado K., Shikano M., and Kageyama H., Tatsumi K., Material design concept for Fe-substituted Li_2MnO_3 -based positive electrodes, *J. Power Sources*, 2007, **174** (2): 554.
- [13] HU C.Y., Li Z., Guo J., Du Y., Wang X.Y., Liu X., and Yi T., Synthesis and electrochemical properties of $\text{Li}[\text{Ni}_x\text{Co}_y\text{Mn}_{1-x-y}]\text{O}_2$ ($x, y= 2/8, 3/8$) cathode materials for lithium ion batteries, *Rare Metals*, 2009, **28**(1): 43.
- [14] Li T., Qiu W.H., Zhao H.L., and Liu J.J., Effect of lithium content on the electrochemical properties of solid-state-synthesized spinel $\text{Li}_x\text{Mn}_2\text{O}_4$, *Rare Metals*, 2007, **26**(3): 280.
- [15] Boulineau A., Croguennec L., Delmas C., and Weill F., Structure of Li_2MnO_3 with different degrees of defects, *Solid State Ionics*, 2010, **180**: 1652.
- [16] Kosova N.V., Devyatkina E.T., Kaichev V.V., and Slobodnyuk A.B., From 'core-shell' to composite mixed cathode materials for rechargeable lithium batteries by mechanochemical process, *Solid State Ionics*, 2011, **192**: 284.
- [17] Lin Y., Zeng B. Z., Lin Y.B., Li X.W., Zhao G.Y., Zhou T., Lai H., and Huang Z.G., Electrochemical properties of carbon-coated LiFePO_4 and $\text{LiFe}_{0.98}\text{Mn}_{0.02}\text{PO}_4$ cathode materials synthesized by solid-state reaction, *Rare Metals*, 2012, **31** (2): 145.
- [18] Liu J.J., Qiu W.H., Yu L.Y., Zhao H.L., and Li T., Synthesis and electrochemical characterization of layered $\text{Li}(\text{Ni}_{1/3}\text{Co}_{1/3}\text{Mn}_{1/3})\text{O}_2$ cathode materials by low-temperature solid-state reaction, *J. Alloys Compd.*, 2008, **449** (1-2): 326.
- [19] Wei G.Z., Lu X., Ke F.S., Huang L., Li J.T., Wang Z.X., Zhou Z.Y., and Sun S.G., Crystal habit-tuned nanoplate material of $\text{Li}[\text{Li}_{1/3-2x/3}\text{Ni}_x\text{Mn}_{2/3-x/3}]\text{O}_2$ for high-rate performance lithium-ion batteries, *Adv. Mater.*, 2010, **22** (39): 4364.
- [20] Villepin De J., and Novak A., Neutron inelastic scattering spectra of strongly hydrogen bonded acid oxalates NaHC_2O_4 , KHC_2O_4 and LiHC_2O_4 , *Chem. Phys.*, 1980, **48** (1): 113.
- [21] Coats A.W., and Redfern J.P., Kinetic parameters from thermogravimetric data, *Nature*, 1964, **201**: 68.
- [22] Malek J., The applicability of Johnson-Mehl-Avrami model in the thermal analysis of the crystallization kinetics of glasses, *Thermochim. Acta*, 1995, **267**: 61.
- [23] Malek J., Kinetic analysis of crystallization processes in amorphous materials, *Thermochim. Acta*, 2000, **355**: 239.